https://doi.org/10.18321/ectj1437

Investigation of Synthesis and Deposition Methods for Cesium-Based Perovskite Quantum Dots for Solar Cell Applications

B. Davletiyarov[1], K. Akmurzina[1], A. Seralin[2], G. Bizhanova[1], B. Baptayev[2], M. Balanay[3], A. Ng[1,2]*

[1]Department of Electrical and Computer Engineering, School of Engineering and Digital Sciences, Nazarbayev University, Kabanbay Batyr Ave. 53, Nur-Sultan, Kazakhstan
[2]National Laboratory Astana, Kabanbay Batyr Ave. 53, Nur-Sultan, Kazakhstan
[3]Department of Chemistry, School of Sciences and Humanities , Nazarbayev University, Kabanbay Batyr Ave. 53, Nur-Sultan, Kazakhstan

Article info

Received:
15 June 2022

Received in revised form:
27 July 2022

Accepted:
5 October 2022

Keywords:
Perovskites, Quantum dots, Hot injection, Recycling, Deposition, Synthesis, Thin films.

Abstract

The $CsPbI_2Br$ perovskite quantum dots (PQDs) have great potential in photovoltaic applications due to their phase stability and optoelectronic properties. In this work, the synthesis technique of $CsPbI_2Br$ PQDs with the investigation of their properties and applications are identified. The critical issues and precautions for preparing PQDs are also discussed. It is also interesting to find that the collected supernatant solutions during the purification of PQDs can be recycled for preparing other types of PQDs. Meanwhile, this work demonstrates different approaches (i) thermal annealing, usage of (ii) methyl acetate and (iii) ethyl acetate as anti-solvents for preparing $CsPbI_2Br$ PQDs in the form of thin films on glass substrates. The obtained samples are characterized in terms of morphology, structural and optical properties. The results of this work can provide useful information for researchers, particularly for those who are starting to synthesize PQDs for fabrications of solid-state devices.

1. Introduction

Recently, the cost-effective organometal halide perovskite materials with a general chemical formula ABX_3 (A – a monovalent organic or metal cations (e.g. $CH_3NH_3^+$, $NH_2CH{=}NH_2^+$, or Cs^+), B – a divalent metallic cation (Pb^{2+}, Sn^{2+}, Cu^{2+}, etc.), X – halogen anion (F^-, I^-, Br^-, Cl^-, etc.)) have demonstrated promising photovoltaic properties [1–4]. This class of materials demonstrates excellent optoelectronic material properties [5], in terms of tunable bandgap, large absorption coefficient, low binding energy, long carrier diffusion lengths and high carrier mobility etc., leading to the accomplishment of perovskite solar cells (PSCs) with impressive power conversion efficiencies (PCEs) [6–9]. The PSCs show a rapid PCE growth rate among emerging photovoltaics. According to the recent announcement from National Renewable Energy Laboratory (NREL), the single-junction PSC and monolithic perovskite/silicon (Si) tandem have achieved the record PCEs of 25.7% and 31.3%, respectively [10], which are highly comparable to the commercialized photovoltaics (PVs) such as crystalline Si and gallium arsenide (GaAs) etc. Nevertheless, the stability and lifetime of PSCs should be significantly enhanced, so that the devices can be operated for at least for year scales (e.g. 25 years for Si PVs) under the atmosphere ambient with temperature cycling and full exposure to the sunlight.

All-inorganic perovskites, such as cesium-based perovskites, are composed of inorganic components without organic cations. This type of perovskite has higher thermal stability, excellent carrier migration, low exciton binding energy compared to the organic cation containing perovskites [1, 11]. Recently, perovskite nanocrystals such as PQDs have attracted attention from the community due to the quantum-size effects, which enhance their phase stability and exhibit different optical

*Corresponding author.
E-mail addresses: annie.ng@nu.edu.kz

properties compared to the bulk counterparts [12, 13]. PQDs demonstrate high photoluminescence (PL) quantum yield, high defect tolerance, quantum confinement effect, and easily tunable bandgap throughout the entire visible spectra region [1, 14, 15]. The versatile surface chemistry of PQDs allows them to be dispersed in various solvents, which opens up opportunities for different applications [16]. The colloidal synthesis of PQDs can be also compatible for future large-scale industrial processing. This paper aims to report the detailed synthesis procedures of $CsPbI_2Br$ PQDs. Meanwhile, it is important to point out that the supernatant solutions, which are obtained during purification can be used for preparing other types of PQDs. The collected supernatant solutions during the purification of red-emitting $CsPbI_2Br$ QDs can be aged for producing green-emitting QDs. To the best of our knowledge, this is the first demonstration of an effective approach to recycling the wastes generated from the chemical synthesis of PQDs. Furthermore, different deposition methods for preparing PQDs as a compact layer on the glass substrates are compared. The properties of obtained samples were systematically characterized by different techniques.

2. Materials and methods

2.1 Chemicals for $CsPbI_2Br$ PQD synthesis

Lead (II) iodide (PbI_2, 99.999%), lead (II) bromide ($PbBr_2$, 99.99%), 1-octadecene (1-ODE, technical grade, 90%), cesium carbonate (Cs_2CO_3), oleic acid (OA, 90%), oleylamine (OLA, 70%), methyl acetate (MeOAc, anhydrous 99.5%), ethyl acetate (EtOAc, ACS reagent 99.5%), n-hexane (anhydrous 95%), n-octane (anhydrous 99%), chlorobenzene (CB, anhydrous 99.8%), 4-tert butylpyridine (TBP, 98%), bis(trifluoromethane)sulfonimide lithium salt (Li-TFSI, 99.95%), acetonitrile (anhydrous 99.8%) were purchased from Sigma-Aldrich without further treatments. 2,2′,7,7′-Tetrakis(N,N-di-p-methoxyphenylamino)-9,9′-spirobifluorene (Spiro-MeOTAD, >99.5%) was purchased from Lumtec.

2.2 Synthesis of $CsPbI_2Br$ PQDs

2.2.1 Cs-Oleate synthesis

0.407 g of Cs_2CO_3, 1.250 mL of oleic acid (OA), and 20 mL of 1-octadecene (ODE) were put into a 100 mL three-neck flask and dried under N_2 at 120° for 30 min. After that, the Cs-Oleate solution was kept in 90° water with an N_2-filled atmosphere before further use.

2.2.2 $CsPbI_2Br$ precursor preparation and hot injection

0.101 g of $PbBr_2$, 0.311 g of PbI_2 and 25 mL of ODE were placed in another 100 mL three-neck flask and heated under vacuum at 120° for 30 min. Then 2.5 mL of OA and 2.5 mL of OLA were injected into the flask, followed by further treatment under vacuum for 30 min at 120°. When the solution became clear and transparent, it was degassed under N_2 and the temperature was increased to 170°. As soon as it reached the required temperature, previously prepared 2 mL Cs-Oleate was quickly injected into the flask (Fig. 1). The flask was immediately placed in an ice bath until it reached room temperature.

2.2.3 $CsPbI_2Br$ PQD purification

The PQD Purification process was performed in 3-steps: 15 mL of synthesized $CsPbI_2Br$ PQD solution was mixed with 35 mL of MeOAc (i), and centrifuged for 6000 or 9000 rpm for 6 min. The supernatant was discarded after this step for further inspection, and the precipitate was then dispersed in 5 mL hexane, followed by adding 7 mL of MeOAc (ii) with centrifugation for 6000 or 9000 rpm for 6 min. After that, the supernatant was also collected, and the precipitate was re-dispersed in 15 mL of hexane (iii), followed by centrifugation at 6000 or 9000 rpm for 6 min. The supernatant with PQDs was stored overnight at 2 °C in the dark, to precipitate excess Cs and Pb oleates. Finally, the hexane was evaporated on the rotary evaporator, for the final product weight calculation. The precipitate then was redispersed in octane with a concentration of ~75 mg/mL, and ready for further use and investigation. The collected supernatant solution was placed into the laboratory ambient environment under 40 °C without light for 6 days.

2.3 Device Fabrication

The device fabrication process for PSCs follows the device architecture of FTO/ETL/Perovskite/spiro-MeOTAD/Au. FTO substrates went through a 4-step cleaning process in an ultrasonic bath (15 min each step) in 4 solutions: detergent DI

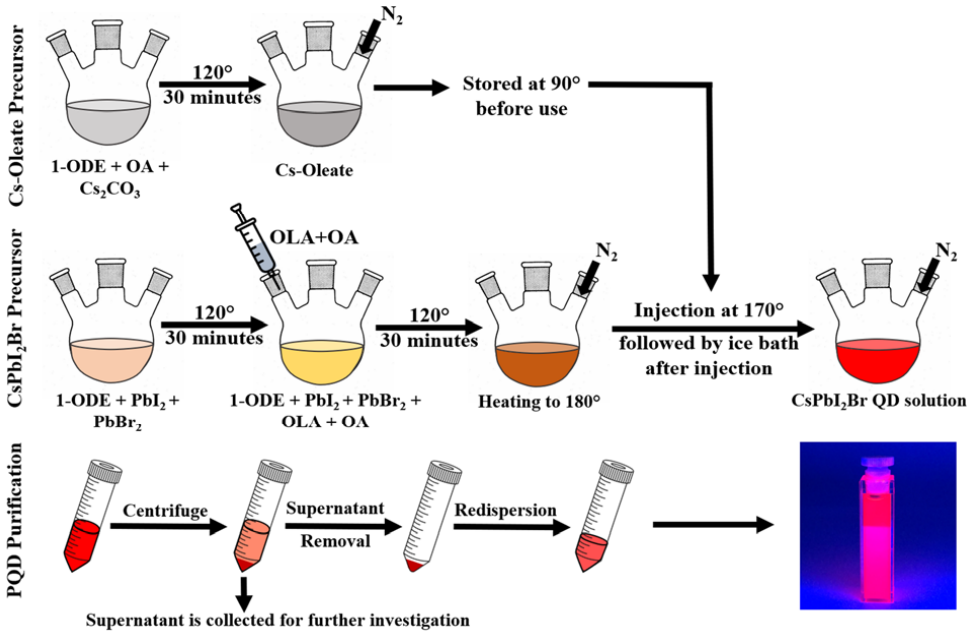

Fig. 1. The schematic representation of PQD synthesis and purification.

water, DI water, acetone, and isopropanol. Before using, the pre-cleaned FTO glasses were treated in UV ozone for 15 min.

2.3.1 Electron-transport layer (ETL) preparation

Commercial zinc oxide nanoparticle ink (2.5 wt.%, dispersed in isopropanol and propylene glycol) was spin-coated on the FTO glass substrates at 3000 rpm for 30 s, followed by thermal annealing for 1 min at 120 °C to obtain the ETL with a thickness of ~50 nm.

2.3.2 Deposition methods of the perovskite layer

As-synthesized PQD solutions are pre-filtered before usage. The $CsPbI_2Br$ PQDs dispersed in octane are spin-coated using three different techniques: (i) thermal annealing – dropping the PQD solution on a substrate and spin-coating at 1000 rpm for the 20 s and 2000 rpm for 10 s, followed by thermal annealing at 130° for 10 min, (ii) usage of methyl acetate (MeOAc) as antisolvent – dropping the PQD solution on a substrate and spin-coating at 1000 rpm for the 20 s and 2000 rpm for 10 s, followed by MeOAc application as an antisolvent, and (iii) usage of ethyl acetate (EtOAc) as antisolvent – depositing the PQD solution on a substrate and spin-coating at 1000 rpm for the 20 s and 2000 rpm for 10 s, followed by EtOAc application as an antisolvent. Depositions are repeated 11–20 times to yield a necessary layer thickness of 200–400 nm.

2.3.3 Hole-transport layer preparation and electrode deposition

The hole-transport layer (HTL) was deposited by spin-coating at 3000 rpm for 30 s the solution of 80 mg of spiro-MeOTAD in 1 mL of CB, 29 µl of tBp, and 17.5 µl of lithium salt. The lithium salt was prepared by dissolving 520 mg of Li-TFSI in 1 mL of acetonitrile. The 70 nm of gold electrodes were thermally evaporated on the HTL layer under the vacuum of 10^{-6} Torr.

2.4 Characterizations

The morphological structure of the $CsPbI_2Br$ PQD was obtained under a Scanning Electron Microscope (Crossbeam 540), Transmission Electron Microscope (JEOL JEM 1400 Plus) and Atomic Force Microscopy (SmartSPM 1000). The crystal structure of the sample is investigated by applying X-ray diffraction system Smartlab (Rigaku). The current-voltage (I-V) measurements were obtained using KeySight B1500A Semiconductor Device Analyzer equipment under simulated AM 1.5G irradiation (100 mW/cm^2) from Sol3A Oriel Newport solar simulator. The I-V measurements were performed in the ambient air. The steady-state photoluminescence (PL) spectra were conducted by using an Edinburgh FLSP920 spectrophotometer. The UV-Vis absorption spectra were measured via Lambda 1050 UV/VIS/NIR Spectrometer (Perkin Elmer).

3. Results and discussion

The hot injection method, introduced by Protesescu et al. [16], takes advantage of the synthesis of PQDs over other methods due to the operation in high temperatures and nitrogen-filled inert environment, which are desired for crystallization of PQDs and enhanced phase stability. This approach has also higher flexibility in controlling the size of the resulting PQDs [1, 3, 5, 14, 15, 17]. During the process, the $CsPbI_2Br$ QDs are formed by the reaction of Cs-Oleate with lead (II) iodide and lead (II) bromide in a high-boiling point solvent (1-octadecene, 1-ODE) at the temperature range of 120–170 °C. The mixture of oleic acid (OA) and oleylamine (OLA) are added into the lead (II) halide precursor during synthesis to afford monodispersion and cubic-phase stability of resulting QDs [18]. Figure 1 represents each step of PQD synthesis and purification. The final PQD structure formation is initiated with a quick injection of the Cs-Oleate into the lead (II) halide precursor solution under high temperature (170 °C), followed by the immersion of the flask into an ice bath for rapid cooling to room temperature. The resultant PQD-containing solution is further purified to remove excess surfactants and unreacted precursors, as PQDs are capped with long alkyl chains, which decrease the electrical properties due to the creation of energy barriers against charge transportation [19]. An one-cycle purification with methyl acetate still leaves excess ligands on the surface of PQDs, hence, at least three cycles of purification should be performed with methyl acetate and hexane [20]. This purification process can agglomerate PQDs during centrifugation and remove excessive ligands properly. Finally, the purified PQDs with reduced surface bound oleate ligands are dispersed in non-polar solvent such as octane with a concentration of ~75 mg/mL for device fabrication.

It is noteworthy that this synthesis approach requires rapid cooling with an ice bath, which will be challenging to perform during large-scale productions. Instead, modifications of temperature control for high volume synthesis will be recommended by using liquid nitrogen or helium to accelerate the cooling rates. The current experiment conditions of synthesis and purification conducted in low air humidity (RH: 10%) so that the $CsPbI_2Br$ QDs in a stable cubic phase can be obtained. The large consumption of solvents and the waste generation are also concerns for future large-scale manufacturing. It is found that the supernatant solution which

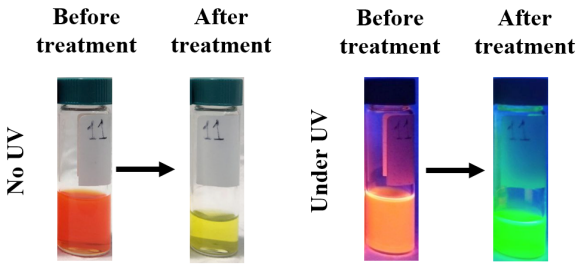

Fig. 2. The supernatant solutions before and after treatment.

is collected during PQD purification can be aged at 40 °C to obtain other types of PQDs. Figure 2 demonstrates the supernatant solution collected during the purification of PQDs before and after treatment. It is observed that the applied heat treatment and aging effect result in the transition of supernatant from red-emitting to green-emitting solution under UV illumination as shown in Fig. 2, which indicates the presence of different types of perovskite nanostructures in the supernatant solution. Figure 3a and 3b show the images from the transmission electron microscopy (TEM) for the perovskite nanostructures contained in the supernatant before and after treatment, respectively. The large spherical nanostructures are observed from the initial supernatant solution while the nanostructures are transformed to a cubic structure with a size of 9 nm ± 1 nm after treatment of the supernatant. The inset of Fig. 3b shows that the obtained nanocrystal has a lattice spacing of 0.310 nm which corresponds to (110) facets of the cubic $CsPbBr_3$ [21]. To characterize the light emission properties of the obtained perovskite nanostructures, the photoluminescence (PL) signals emitted from the samples are investigated. The PL spectra emitted from the samples of $CsPbI_2Br$ QDs, the supernatant before and after treatment are shown in Fig. 3c. The reported bandgap of $CsPbI_2Br$ and $CsPbBr_3$ is ~ 1.9 eV and ~ 2.3 eV respectively [22], which are consistent with the PL peaks located at 650 nm and 527 nm for the sample of the hot-injection synthesized $CsPbI_2Br$ QDs and the product of the supernatant after treatment. The PL peak of the supernatant solution before treatment is located at 618 nm, which is attributed to the presence of a mixture of $CsPbI_xBr_{3-x}$. The values of full width at half maximum (FWHM) of the PL signals are 30, 39 and 31 for the samples of $CsPbI_2Br$ QDs, the supernatant before and after treatment, respectively. A reduction of FWHM from 39 to 31 for the sample of supernatant solution before and after treatment is also an indication of the transformation of $CsPbI_xBr_{3-x}$ mixture to relatively pure $CsPbBr_3$.

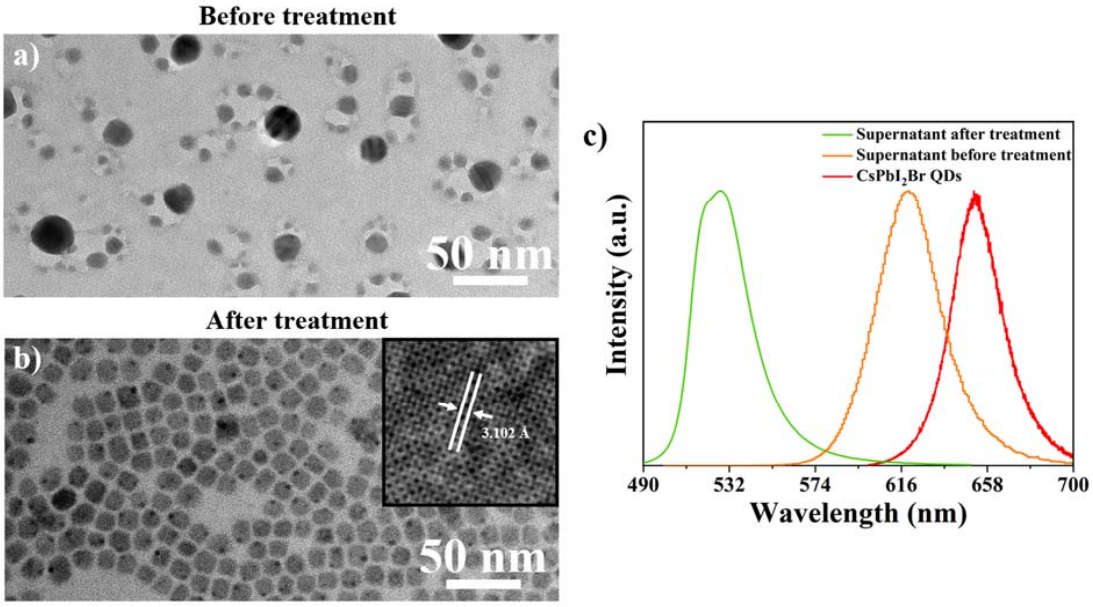

Fig. 3. TEM imaging of supernatant solutions (a) before and (b) after treatment, (c) PL peaks of supernatant before/after treatment and hot-injection synthesized $CsPbI_2Br$ QDs.

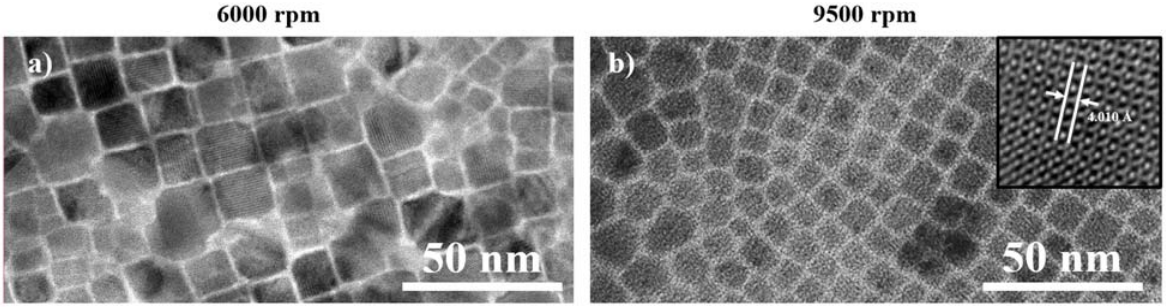

Fig. 4. The TEM images for $CsPbI_2Br$ PQDs with (a) 6000 and (b) 9500 RPM centrifuge speed.

Meanwhile, TEM was performed to investigate the morphology of hot-injection synthesized PQDs. Figure 4 shows the images of PQDs extracted by using 2 different centrifugation speeds (6000 rpm or 9500 rpm) during the purification process. It is observed that the use of a higher centrifugation speed results in more uniform size distribution of PQDs compared to the sample obtained from using a centrifugation speed of 6000 rpm. The size of PQDs obtained from centrifugation speed of 9500 rpm is 9 nm ± 2 nm with a well-resolved lattice spacing of 0.401 nm (Fig. 4b inset) which corresponds to (110) facets of cubic $CsPbI_2Br$ [23] which is consistent to other reported results [24, 25, 26]. It is noteworthy that the resultant QD size and optical properties can be changed by varying the injection temperatures [27].

The PQDs are usually used in optoelectronics such as PSCs as a light-absorption layer. The quality of the deposited layer directly affects the photovoltaic properties of the light-absorption layer and the performance of PSCs. Therefore, it is important to investigate the techniques which can prepare high-quality PQD films on the substrates. In this work, the $CsPbI_2Br$ PQDs were deposited on laboratory glasses by a spin-coating method. Three different deposition techniques were used to remove the solvents: 1) thermal annealing, 2) using methyl acetate (MeOAc) or 3) ethyl acetate (EtOAc) as an anti-solvent. The morphology of the PQD films was investigated by scanning electron microscopy (SEM). Figure 5 demonstrates top-view and cross-sectional SEM images of $CsPbI_2Br$ PQD layers deposited by using three different techniques.

The thermal annealing technique was performed through spin-coating the PQD dispersion solution, followed by the annealing on a hotplate at 130° to evaporate the solvents. Despite the fact that thermal annealing is a straightforward process and it can reduce the defects from the surface of the PQD layer [28], this technique demonstrated a serious coalescence of PQDs instead of forming

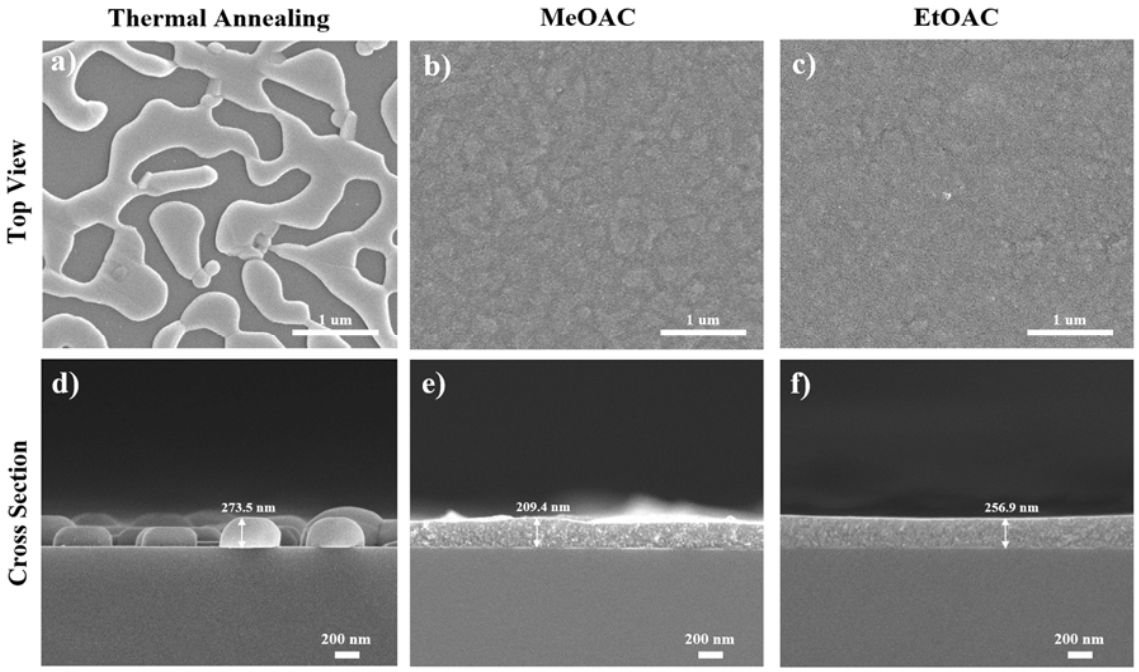

Fig. 5. The SEM (a, b, c) top and (d, e, f) cross-sectional images of $CsPbI_2Br$ PQDs deposited with three different techniques (thermal annealing, using methyl acetate (MeOAc) or ethyl acetate (EtOAc) as an anti-solvent).

a uniform layer (Fig. 5 (a), (d)) due to gradually slow evaporation of residual solvents from the sample during thermal annealing. On the other hand, MeOAc or EtOAc can be used as anti-solvents due to their chemical compatibility with the oleate ligand [4, 29]. During the film preparation process, PQDs dispersed in octane are spin-coated on the substrate and followed by dripping MeOAc or EtOAc on the surface of the spinning sample. It is proposed that the application of MeOAc and EtOAc as anti-solvents during spin coating can improve QD coupling [8], along with the removal of excess surface ligands [30]. Based on the SEM images as shown in Fig. 2b-2f, pinhole-free compact layers are uniformly deposited on the glass substrates by using the antisolvent technique during the spin-coating process. In this work, the spinning processes were repeated 20 times in order to obtain a layer thickness of ~200 nm. To analyze the PQD structure and crystallization, X-ray diffraction (XRD) measurement was performed as shown in Fig. 6. We can find that the prominent diffraction peaks located at 14.5° and 29.2° are corresponding to the crystal planes of [100] and [200], which consistently indicate the cubic phase of $CsPbI_2Br$ PQDs [31].

The surface roughness of PQD films prepared by different anti-solvents during the spin-coating process were further investigated by atomic force microscopy (AFM) as shown in Fig. 7. The root mean square (RMS) roughness of the $CsPbI_2Br$ PQD films prepared by using EtOAc and MeOAc anti-solvents are found to be 46.3 nm and 111.1 nm, respectively. The AFM results show that the use

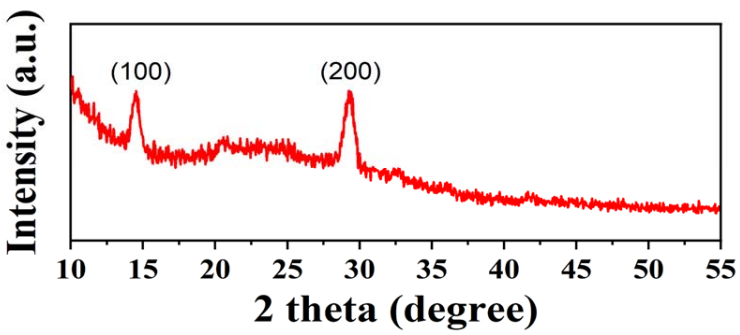

Fig. 6. The typical XRD patterns of $CsPbI_2Br$ PQD film prepared by using an antisolvent during the spin-coating process.

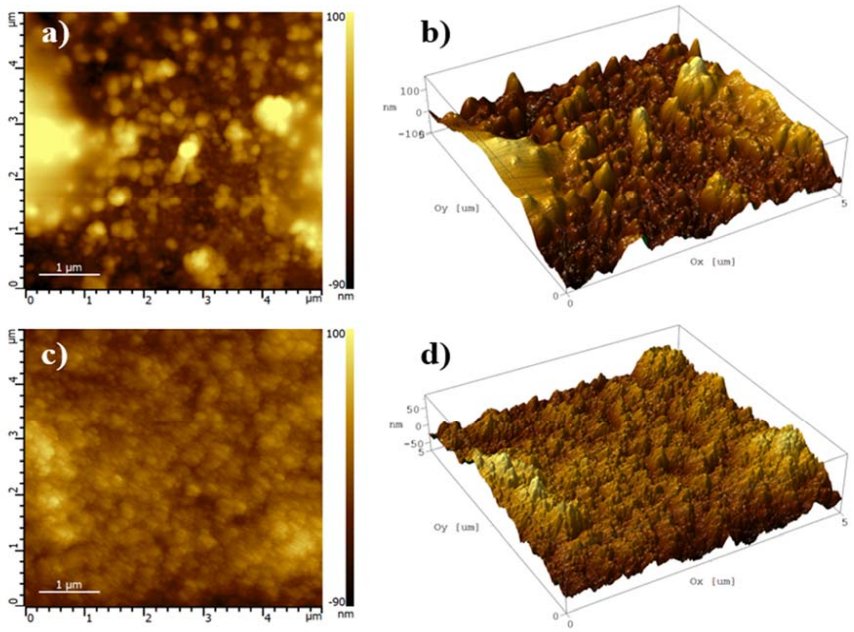

Fig. 7. The AFM imaging was obtained from $CsPbI_2Br$ PQD films prepared by using (a) (b)MeOAc and (c) (d) EtOAc as the antisolvent during the spin coating process.

of EtOAc as an antisolvent during the spin-coating process yields the PQD film with a smoother surface compared to the film treated with MeOAc anti-solvent. The PQD film with lower surface roughness is desired for application in PSCs as it can form better contact with other functional layers (e.g. carrier transport layers) in the devices.

The optical properties of $CsPbI_2Br$ PQDs were investigated by photoluminescence (PL) and UV-Vis absorption measurements. The characterizations were performed on PQDs in dispersion solution and the form of the solid film deposited on the glass substrate (Fig. 8). The absorption properties of PQDs are shown in Fig. 8a while the absorption edge can be extracted by the Tauc plot as shown in Fig. 8b. It is found that the absorption edge of PQDs in dispersion solution is located at 1.89 eV which is consistent with the previous reports [32] for $CsPbI_2Br$ material. It is noteworthy that a blue-shift in absorption edge (~0.3 eV) is observed for PQD thin film. As for the emission properties, the sample of PQDs dispersed in octane exhibits the PL peak at 652 nm, while the peak of PQDs in solid film locates at 644 nm (Fig. 8b). The blue-shift in the absorption edge and PL peak of the PQD film can be attributed to the presence of impurities and surface defects [33]. In a previous study, it was demonstrated that a replacement of Cs^+ with a smaller ionic metal such as Rb^+ results in a blue-shift of PL peak [34, 35]. This is due to the fact that Pb-Cl-Pb in $CsPbCl_3$:Rb QDs is more distorted leading to the overlap of the antibonding orbital electron clouds of the Pb^{2+} and halide anion which weakens the bond interaction and results in

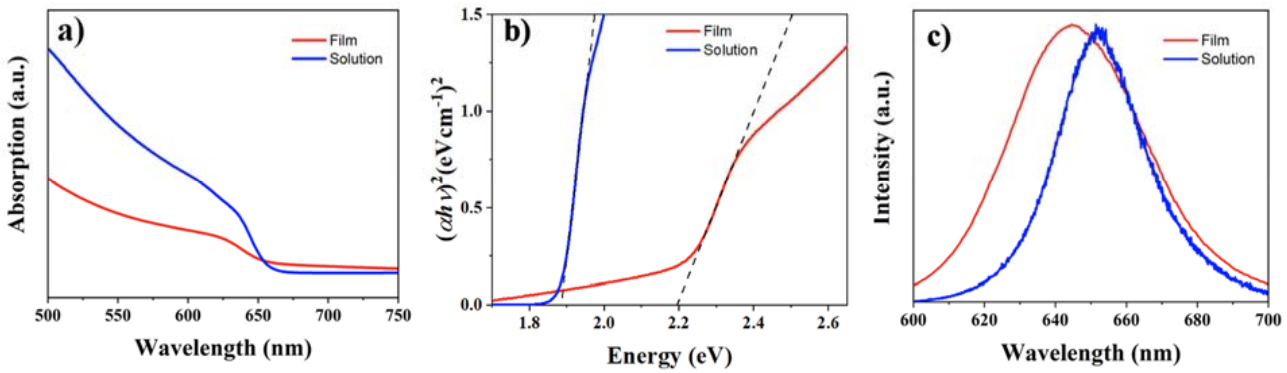

Fig. 8. (a) The absorption, (b) Tauc plot and c) PL results of the solution-based and film-based $CsPbI_2Br$ QDs.

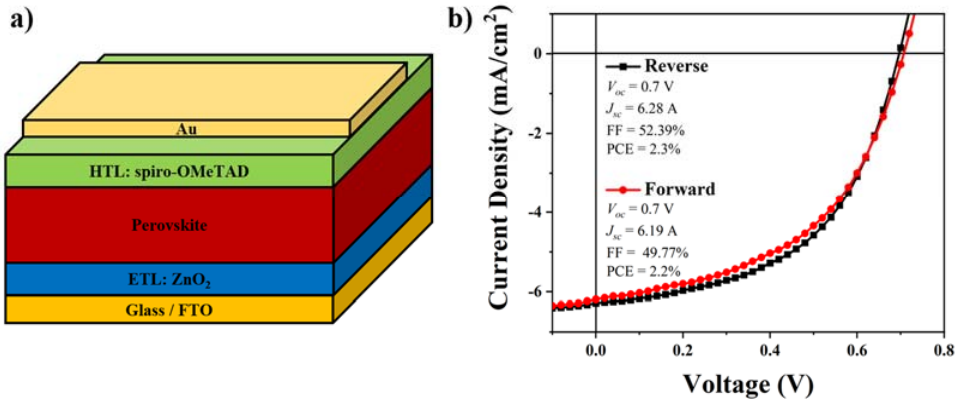

Fig. 9. (a) The device architecture of a PQDSC and (b) JV curve of the fabricated PQDSC.

a wider band gap of materials. In another study of CuInSe QDs, the broad bandwidth of emissions is characterized by defect-radiative transitions. In addition, inhomogeneity in the size of the QDs could also lead to such broadening effects [33]. This type of analogies can be used to explain our observation that the presence of impurities could weaken the Cs-X-Cs or Pb-X-Pb interactions thus producing a blue-shift and the existence of surface defects and/or inhomogeneity of the thin film system cause a broader PL spectrum.

The PSC devices with an architecture of FTO/ZnO_2/PQDs/spiro-OMeTAD/Au (Fig. 9a) were fabricated. Figure 9b shows the typical J-V curve of the perovskite quantum dot solar cells (PQDSC) based on $CsPbI_2Br$. It is noted that the existing reports on PSCs using all-inorganic PQDs as the active layer are based on $CsPbI_3$, which exhibit the PCEs from ~10% to 16% [27, 36] while the PSCs based on mixed halide composition such as $CsPbI_xBr_{3-x}$, exhibit significantly lower PCEs (below 10%) [37–39]. It could be due to the high density of surface defects of PQDs as speculated from the PL results (Fig. 8b) as well as non-optimized interfacial quality between carrier transport layers and PQDs. Since the PQDSCs based on all-inorganic mixed halide composition are less explored, it is believed that the obtained PCE of the device in this work still has a lot of room to be enhanced. Future works can be focused on different surface passivation techniques [40–42] and the architecture engineering of PQDSCs [43, 44].

4. Conclusion

The details of the synthesis and deposition methods of $CsPbI_2Br$ QDs are reported in this work. The temperature and the inert ambient for the hot-injection process should be carefully controlled to yield PQDs with high reproducibility while the centrifuge speed should be high enough in order to extract the uniform size of PQDs. The morphology of the solid film composed of PQDs is significantly affected by different deposition methods. It is found that the use of EtOAc as an antisolvent during the spin-coating process can reduce the surface roughness of the resultant PQD solid films. The performed characterizations exhibit the material properties of the obtained PQDs. The PQDSC based on $CsPbI_2Br$ as an active layer yields a PCE of 2.3% in this work. Implementation of surface passivation and architecture engineering should be further investigated for enhancing the performance of PQDSCs based on all-inorganic mixed halide composition. On the other hand, this work also proposes a recycling strategy for the supernatant generated from the purification of $CsPbI_2Br$ QDs. The green emissive $CsPbBr_3$ QDs with a uniform size of 9 nm ± 1 nm can be obtained from the supernatant aging at 40 °C. This finding can provide a potential solution in the future for recycling the huge amount of wastes generated from the industrial-scale synthesis of PQDs.

Acknowledgements

A.N. acknowledges the financial support from the Science Committee of the Ministry of Education and Science of the Republic of Kazakhstan (Scientific Research Grant no. AP08856931, AP14869983) and Nazarbayev University (Grant no. 021220CRP0422).

References

[1]. F. Bella, P. Renzi, C. Cavallo, C. Gerbaldi, *Chem.-Eur. J.* 24 (2018). 12183–12205. DOI: 10.1002/chem.201801096

[2]. W. Chen, X. Li, Y. Li, Y. Li, *Energy Environ. Sci.* 13 (2020) 1971–1996. DOI: 10.1039/d0ee00215a
[3]. W. Chi, S.K. Banerjee, *Small* 16 (2020) 1907531. DOI: 10.1002/smll.201907531
[4]. C. Lee, Y. Shin, G.G. Jeon, D. Kang, et al., *Energies* 14 (2021) 201. DOI: 10.3390/en14010201
[5]. Z. Qiu, N. Li, Z. Huang, Q. Chen, et al., *Small Methods* 4 (2020) 1900877. DOI: 10.1002/smtd.201900877
[6]. L. Liu, A. Najar, K. Wang, M. Du, et al., *Adv. Sci.* 9 (2022) 2104577. DOI: 10.1002/advs.202104577
[7]. R. Syah, A. Davarpanah, M.K.M. Nasution, Q. Wali, et al., *Coatings* 11 (2021) 1173. DOI: 10.3390/coatings11101173
[8]. E.A. Erazo, H.E. Sánchez-Godoy, A.F. Gualdrón-Reyes, S. Masi, et al., *Nanomaterials* 10 (2020) 1586. DOI: 10.3390/nano10081586
[9]. C. Liu, M. Hu, X. Zhou, J. Wu, et al., *NPG Asia Mater.* 10 (2018) 552–561. DOI: 10.1038/s41427-018-0055-0.
[10]. NREL, Https://Www.Nrel.Gov/Pv/Cell-Efficiency.Html, Best Research-Cell Efficiency Chart (2022).
[11]. H. Li, T. Luo, S. Zhang, Z. Sun, et al., *Energy and Environmental Materials* 4 (2021) 46–64. DOI: 10.1002/eem2.12087
[12]. W. Chi, S.K. Banerjee, *Angew. Chem*. 134 (2022) e202112412. DOI: 10.1002/ange.202112412
[13]. R.X. Yang, L.Z. Tan, *J. Chem. Phys.* 152 (2020) 034702. DOI: 10.1063/1.5128016
[14]. J. Chen, D. Jia, E.M.J. Johansson, A. Hagfeldt, et al., *Energy Environ. Sci.* 14 (2021) 224–261. DOI: 10.1039/d0ee02900a
[15]. B. Chaudhary, Y.K. Kshetri, H.S. Kim, S.W. Lee, et al., *Nanotechnology* 32 (2021). DOI: 10.1088/1361-6528/ac2537.
[16]. L. Protesescu, S. Yakunin, M.I. Bodnarchuk, F. Krieg, et al., *Nano Lett.* 15 (2015) 3692–3696. DOI: 10.1021/nl5048779
[17]. H. Wang, H. Bian, Z. Jin, H. Zhang, et al., *Chem. Mater.* 31 (2019) 6231–6238. DOI: 10.1021/acs.chemmater.9b02248
[18]. J. Kim, S. Cho, F. Dinic, J. Choi, et al., *Nano Energy* 75 (2020) 104985. DOI: 10.1016/j.nanoen.2020.104985
[19]. Y. Wang, J. Yuan, X. Zhang, X. Ling, et al., *Adv. Mater.* 32 (2020) 2000449. DOI: 10.1002/adma.202000449
[20]. R. Han, Q. Zhao, J. Su, X. Zhou, et al., *J. Phys. Chem. C* 125 (2021) 8469–8478. DOI: 10.1021/acs.jpcc.0c09057
[21]. X. Zhang, H.C. Wang, A.C. Tang, S.Y. Lin, et al., *Chem. Mater.* 28 (2016) 8493–8497. DOI: 10.1021/acs.chemmater.6b04107
[22]. H. Huang, L. Polavarapu, J.A. Sichert, A.S. Susha, et al., *NPG Asia Mater.* 8 (2016). DOI: 10.1038/am.2016.167
[23]. C.J. Thomas, Y. Zhang, A. Guillaussier, K. Bdeir, et al., *Chem. Mater.* 31 (2019) 9750–9758. DOI: 10.1021/acs.chemmater.9b03533
[24]. R. An, F. Zhang, X. Zou, Y. Tang, et al., *ACS Appl. Mater. Interfaces* 10 (2018) 39222–39227. DOI: 10.1021/acsami.8b14480
[25]. Y. Li, X. Wang, W. Xue, W. Wang, et al., *Nano Res*. 12 (2019) 785–789. DOI: 10.1007/s12274-019-2289-8
[26]. Q. Zeng, X. Zhang, C. Liu, T. Feng, et al., *Solar RRL* 3 (2019) 1800239. DOI: 10.1002/solr.201800239
[27]. A. Swarnkar, A.R. Marshall, E.M. Sanehira, B.D. Chernomordik, et al., *Science* 354 (2016) 92–95. DOI: 10.1126/science.aag2700
[28]. S.Y. Lien, P.J. Lai, W.R. Chen, C.H. Liu, et al., *Crystals* 12 (2022). DOI: 10.3390/cryst12020204
[29]. S. Rühle, *Solar Energy* 130 (2016) 139–147. DOI: 10.1016/j.solener.2016.02.015
[30]. H. Chen, M. Li, B. Wang, S. Ming, et al., *J. Alloy. Compd.* 862 (2021) 158442. DOI: 10.1016/j.jallcom.2020.158442
[31]. P. Cottingham, R.L. Brutchey, *Chem. Mater.* 28 (2016) 7574–7577. DOI: 10.1021/acs.chemmater.6b03553
[32]. J. Zhou, F. Huang, H. Lin, Z. Lin, et al., *J. Mater. Chem. C* 4 (2016) 7601–7606. DOI: 10.1039/c6tc02405j
[33]. S.C. Shei, W.J. Chiang, S.J. Chang, *Nanoscale Res. Lett*. 10 (2015) 122. DOI: 10.1186/s11671-015-0789-3
[34]. Z. Zhao, W. Xu, G. Pan, Y. Liu, et al., *Mater. Res. Bull.* 112 (2019) 142–146. DOI: 10.1016/j.materresbull.2018.12.004
[35]. M.R. Linaburg, E.T. McClure, J.D. Majher, P.M. Woodward, *Chem. Mater.* 29 (2017). DOI: 10.1021/acs.chemmater.6b05372
[36]. D. Jia, J. Chen, X. Mei, W. Fan, et al., *Energy Environ. Sci.* 14 (2021) 4599–4609. DOI: 10.1039/d1ee01463c
[37]. D. Ghosh, M.Y. Ali, D.K. Chaudhary, S. Bhattacharyya, *Solar Energy Mater. Sol. Cells* 185 (2018) 28–35. DOI: 10.1016/j.solmat.2018.05.002.
[38]. S. Christodoulou, F. di Stasio, S. Pradhan, A. Stavrinadis, et al., *J. Phys. Chem. C* 122 (2018). 7621–7626. DOI: 10.1021/acs.jpcc.8b01264
[39]. D. Ghosh, Y.M. Ali, A. Ghosh, A. Mandal, et al., *J. Phys. Chem. C* 125 (2021) 5485–5493. DOI: 10.1021/acs.jpcc.0c11122
[40]. L. Hu, Q. Zhao, S. Huang, J. Zheng, et al., *Nat. Commun.* 12 (2021) 466. DOI: 10.1038/s41467-020-20749-1
[41]. J. Khan, X. Zhang, J. Yuan, Y. Wang, et al., *ACS Energy Lett.* 5 (2020) 3322–3329. DOI: 10.1021/acsenergylett.0c01849
[42]. D. Aidarkhanov, Z. Ren, C.K. Lim, Z. Yelzhanova, et al., *Solar Energy Mater. Sol. Cells* 215 (2020) 110648. DOI: 10.1016/j.solmat.2020.110648
[43]. S. Akin, Y. Altintas, E. Mutlugun, S. Sonmezoglu, *Nano Energy* 60 (2019) 557–566. DOI: 10.1016/j.nanoen.2019.03.091
[44]. F. Cheng, R. He, S. Nie, C. Zhang, et al., *J. Am. Chem. Soc.* 143 (2021) 5855–5866. DOI: 10.1021/jacs.1c00852